LANGMUIR
Article
Cite This: *Langmuir* 2019, 35, 3724−3732
pubs.acs.org/Langmuir

Self-Organization of Fluids in a Multienzymatic Pump System

Subhabrata Maiti,[†,§] Oleg E. Shklyaev,[‡,§] Anna C. Balazs,[*,‡] and Ayusman Sen[*,†]

[†]Department of Chemistry, The Pennsylvania State University, 104 Chemistry Building, University Park, Pennsylvania 16802, United States

[‡]Department of Chemical Engineering, University of Pittsburgh, 4420 Bayard Street, Pittsburgh, Pennsylvania 15213, United States

Supporting Information

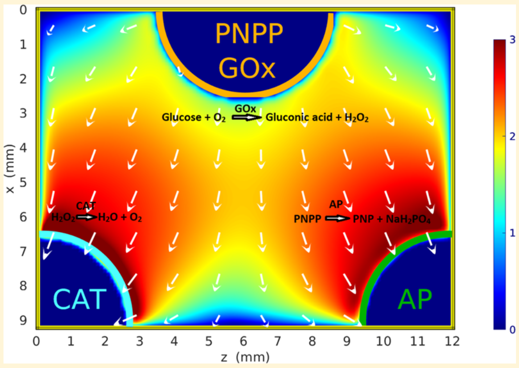

ABSTRACT: The nascent field of microscale flow chemistry focuses on harnessing flowing fluids to optimize chemical reactions in microchambers and establish new routes for chemical synthesis. With enzymes and other catalysts anchored to the surface of microchambers, the catalytic reactions can act as pumps and propel the fluids through the containers. Hence, the flows not only affect the catalytic reactions, but these reactions also affect the flows. Understanding this dynamic interplay is vital to enhancing the accuracy and utility of flow technology. Through experiments and simulation, we design a system of three different enzymes, immobilized in separate gels, on the surface of a microchamber; with the appropriate reactants in the solution, each enzyme-filled gel acts as a pump. The system also exploits a reaction cascade that controls the temporal interactions between two pumps. With three pumps in a triangular arrangement, the spatio-temporal interactions among the chemical reactions become highly coordinated and produce well-defined fluid streams, which transport chemicals and form a fluidic "circuit". The circuit layout and flow direction of each constituent stream can be controlled through the number and placement of the gels and the types of catalysts localized in the gels. These studies provide a new route for forming self-organizing and bifurcating fluids that can yield fundamental insight into nonequilibrium, dynamical systems. Because the flows and fluidic circuits are generated by internal chemical reactions, the fluids can autonomously transport cargo to specific locations in the device. Hence, the findings also provide guidelines to facilitate further automation of microfluidic devices.

■ INTRODUCTION

Understanding how fluid flows affect chemical reactions in solution is vital to optimizing industrial processes and is the focus of the young field of microscale "flow chemistry", which has grown dramatically in the last decade.[1−9] The development of microfluidic devices spurred this growth by enabling researchers to mechanically pump dissolved chemicals into microscopic channels and, thus, rapidly explore new synthetic routes with a small amount of chemicals under controlled flow conditions. Flow chemistry at the microscale is particularly advantageous over "chemistry in a flask" for reactions involving catalysis, an area where flow technology can have a significant impact in both fundamental research and industrial applications.[1] In these microsystems, the catalysts are immobilized on the surface and, thus, can be reused multiple times, leading to less waste and more sustainable processes.[2] Anchored catalysts in a flow chamber, however, introduce a fundamental challenge that only now is being brought to light. Namely, at the microscale, the flow not only affects the catalytic reaction, but the reaction also affects the flow. This point was made evident by Sen et al.,[10−15] who recently showed that enzymes and other catalysts anchored to the wall of a microchamber can act as "chemical pumps": in the presence of the appropriate reactants, the catalytic reactions within the chamber drive the spontaneous flow of the enclosed fluid. Understanding this dynamic interplay between catalytic reactions and the surrounding fluid is critical to advancing the emerging field of microscale flow chemistry.

The finding that immobilized catalysts can pump fluids in a microchamber is, in fact, highly beneficial for the further development of lab-scale flow devices.[16−22] In particular, the use of the external pumps limits the portability and utility of the laboratory devices. Shifting the work of pumping from peripheral mechanical (electrical) machinery to internal chemical reactions has two significant advantages. First, the devices can operate as stand-alone systems that do not require external power. Second, without the externally imposed flow, researchers can probe the inherent interactions in the system and thereby gain insight into the intrinsic feedback between chemistry and flow at the microscale.

Herein, we use both experimental and computational approaches to examine the dynamic interactions between catalytic reactions and fluid flow in a system of three well-separated enzymatic pumps within a fluid-filled microchamber. These chemical pumps generate the flows that transport reactants, which subsequently initiate flows at the neighboring

Received: October 26, 2018
Revised: December 23, 2018
Published: February 5, 2019

DOI: 10.1021/acs.langmuir.8b03607
Langmuir 2019, 35, 3724−3732

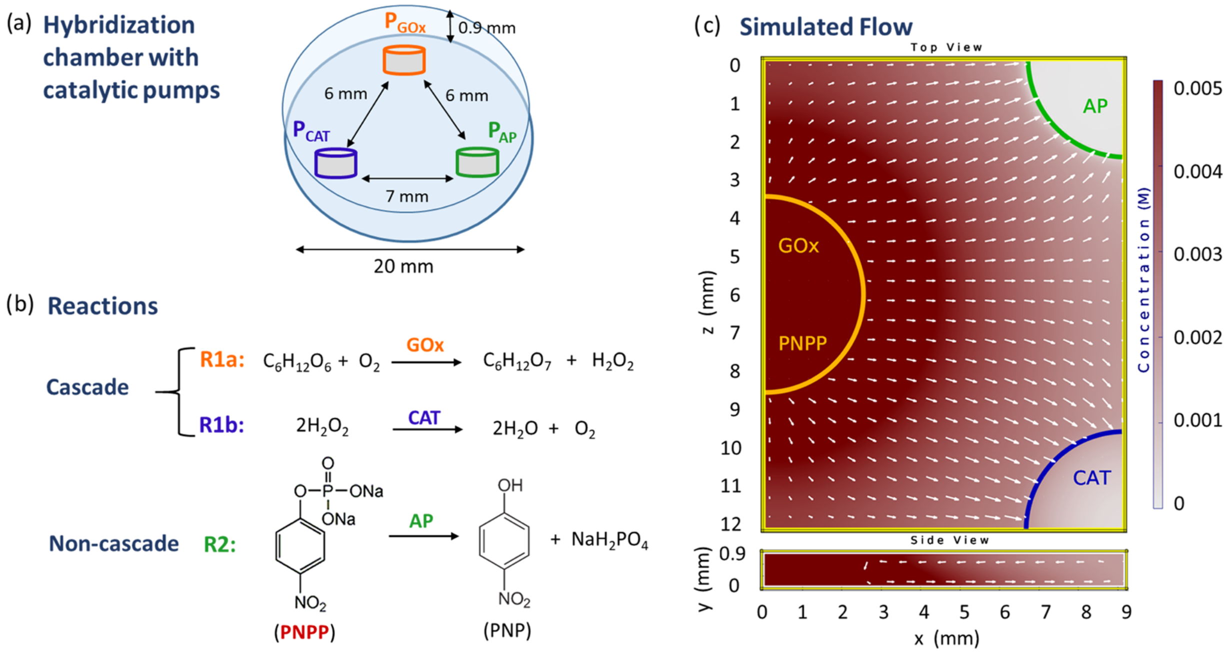

Figure 1. (a, b) Schematic representation of the overall flow behavior in this multienzymatic system and the corresponding reaction schemes. (c) The top and side views of the simulation domain show the concentration of *p*-nitrophenylphosphate (PNPP) (red color map) leaching out of P_{GOx} pump (orange circle), and the directions of the horizontal fluid velocities $u_h = (u_x^2 + u_z^2)^{1/2}$ (white arrows) generated between P_{GOx} and P_{CAT} (P_{AP}) pumps, which are shown with blue and green circles, respectively. The arrows show the direction of the flow in the plane $y = 0.2$ mm for the top view and in the $z = 6$ mm plane for the side view.

pumps. As shown below, the generated flows self-organize into two distinct streams (Figure 1a) and do so without the aid of guiding walls. These bifurcated flows are used to simultaneously deliver microparticles to two different sites. Our findings provide new guidelines for designing self-organizing fluidic circuits that can be controlled by the arrangement, number, and types of pumps. In the addition to yielding fundamental insight into the behavior of nonequilibrium dynamical systems, the study provides much-needed design rules[1] for regulating chemistry in flow. On the basis of these concepts, researchers can devise microscale devices that autonomously carry out multistep chemical reactions, especially in scenarios where the product of one reaction is the reactant for the next. Namely, with a particular configuration of chemical pumps and input of the appropriate initial reactant, the system could execute the desired sequence of reactions in a purely self-sustained manner, generating both the flow and the fluidic circuit that guides this flow.

To facilitate the ensuing discussion, we specify the main components of our system here: the flow and the enzymes. The flows arise due to solutal buoyancy effects, where density differences between reactants and products of the reaction generate gradients, which in turn generate the flow. Due to the continuity of the confined fluid, the flow exhibits circular convection.[23,24] When the products are denser (i.e., occupy less volume) than the reactants, the fluid flows outward, away from an enzyme-coated patch on a bottom surface, whereas fresh solution is drawn from above toward the reactive patch. Conversely, if the products are less dense (occupy more volume) than the reagents, the fluid will rise upward and thus draw fresh solution inward, toward the surface patch. Because the flow velocity is a function of the catalytic turnover rate, it can be controlled by adjusting the concentrations of the reactants and the corresponding immobilized enzymes.

The enzymes are immobilized in three different pieces of agarose gel (see Figure 1a) and act as pumps in the presence of the appropriate substrates. As described below, we determine the mechanisms governing the fluid flow and particle transport in the multipump system. Given the ease of encapsulating species into gels and tailoring the gel placement in the chamber, the platform permits the design of new dynamical systems by combining the actions of chemical pumps. The time scale in our system is set by the rate at which *p*-nitrophenylphosphate (PNPP), which is encapsulated in the glucose oxidase pump (P_{GOx}), is released and the rates of the catalytic chemical reactions R1a, RRR1b, and RRR2, which fuel the fluid motion (Figure 1b). Once the reactions stop (all reactants are transformed), the chemical products become uniformly distributed throughout the domain and the fluid motion stops.

The manuscript is organized as follows. We first examine the behavior of the individual pumps; building on this information, we then examine the interactions between two separated pumps. Finally, we construct the three-pump system. At each stage, the experimental observations were compared to simulations of the comparable system (localized in the fluid-filled rectangular shown box in Figure 1c).

■ EXPERIMENTAL SECTION

Materials and Instrumentation. All commercially available reagents were used as received. Solid agar (ultrapure bioreagent) was procured from JT Baker, Avantor. All of the enzymes, catalase (CAT, Bovine liver), glucose oxidase (from *Aspergillus niger*, G7141), acid phosphatase (AP, from potato, P1146), and horseradish peroxidase (HRP, P8375, Type-VI) were procured from Sigma-Aldrich. The other molecules *p*-nitrophenylphosphate hexahydrate, D-glucose, L-glucose, 2-(*N*-morpholino)ethanesulfonic acid (MES) were procured from Sigma and H_2O_2 from Merck. The polystyrene sulfate particles (2 μm in diameter) were purchased from Polysciences Co. The confined experiment was performed using a secure-seal hybridization chamber procured from Electron Microscopy Sciences.

The UV−vis measurements were performed in a UV−vis spectrophotometer (Thermo Fisher scientific). Optical microscopic images were captured using an optical setup, which comprised a microscope (Zeiss Axiovert 200) with a halogen lamp (100 W) and a 5× or 20× objective lens. Images were recorded using a charge-coupled device camera attached to the optical microscope. The videos were recorded at 200 μm (which is almost 1/4th height compared to the overall 900 μm of the chamber height) above the bottom surface to obtain the maximum fluid velocity.

Gel Preparation. We employed 3% agarose gels as the matrix for the pumps. Specifically, 12 mg of agarose was weighed, and then 400 μL of the total volume of aqueous solution added to make the final concentration of MES (40 mM, pH 6) and L-glucose (42.5 mM) (whenever needed). It was then placed at 120 °C in an oven for 3 min to liquefy. Then, 20 μL of the liquefied gel was added to a mold of 5 mm diameter and allowed to cool to form the gel. For enzyme-containing gels, 50 μL of the enzyme solution and also the PNPP solution, in the case of P_{GOx} was added to the liquefied gel so that the final amount of enzyme and PNPP is as noted (GOx = 56 pmol, CAT = 10 pmol, AP = 110 pmol, and varying PNPP (for P_{GOx}) = 0.6, 1.11, 2.0 μmol in three different sets of experiment). Following that 20 μL of the liquefied enzyme-containing agar solution was pipetted out and placed in the mold to allow it to form the gel.

We incorporated the gel in a covered circular secure-seal hybridization chamber (Electron Microscopy Sciences) with dimensions of 20 mm diameter, 0.9 mm height along with tracer particles for the measurement of the flow velocity.

Visualization of the Tracer Particle Density. We calculated the tracer particle density at the bottom surface of the chamber after 120 min. Below are the snapshots of the particle density at different places along the P_{CAT} and P_{AP} axes. Two sets of experiments were performed. In one case, all of the enzymes were present in the corresponding gels, and D-glucose was present in the solution (as shown in Figure 3). In the other case, there was no CAT and AP in P_{CAT} and P_{AP}, respectively, whereas glucose was present in the solution (as shown in the Supporting Information (SI) Figure S14). The particle density profiles at different zones along the P_{CAT} and P_{AP} axes in both the cases are given in the main manuscript. The images clearly show that the tracers are localized near the activated pumps and are absent in the regions between the pumps. Since the tracers simply follow the flow fields, these results indicate that generated flows are effective at transporting the tracers to specific locations.

Visual Detection of the Bifurcating Flow. We performed an experiment to detect the flow behavior visually in the presence of three gels. The experiment was done in a Petri dish of 5 cm diameter. The images from the experiment taken at different time intervals are in Figure 4c of the manuscript. In this experiment, we put GOx + PNPP in one gel, HRP + 2,2′-azino-bis(3-ethylbenzothiazoline-6-sulfonic acid) diammonium salt (ABTS) in the other gel, and AP in the third gel and placed them in an equilateral triangle arrangement. The concentration of the enzymes and PNPP were similar to the previous flow experiments. The gels have a diameter of 1 cm, and 400 μL of the gel solutions with all of the reagents and enzymes were used to make the cylindrical shapes. The addition of glucose solution results in the formation of H_2O_2 which then diffuses to the HRP-containing gel to oxidize ABTS resulting in a blue color. Thus, we can observe the direction of pumping by following the migration of blue color and its spatial distribution over time. Similarly, the leached PNPP from the GOx gel migrates toward AP-containing gel where a yellow color is formed due to the formation of PNP by enzymatic catalysis.

Numerical Modeling. Previous analyses of various chemical pumps[11,13] showed that despite the exothermicity of the corresponding catalytic reactions, the convective flows were generated primarily by effects due to solutal buoyancy. Therefore, we assume that fluid motion is coupled to the chemical composition of the solution solely through the solutal buoyancy mechanism, and the thermal buoyancy is ignored. In our model, variations in the density of the aqueous solution depend on concentrations C^j of N^C reactants measured relative to corresponding reference values C_0^j $(1 \leq j \leq N^C)$. In particular, a solvent of density ρ_0 undergoes the following change[23]

$$\Delta\rho = \rho_0 \sum_{j=1}^{N^C} \beta_C^j (C^j - C_0^j) \tag{1}$$

The volumetric solutal expansion coefficients β_C^j characterize the magnitude of the density variations in response to changes in solute concentrations $C^j - C_0^j$. The fluid flow is generated by the buoyancy force $\Delta\rho\mathbf{g}$ (with the vector $\mathbf{g}$ describing gravity) that is determined by the properties of the solution as well as the size and geometry of the fluid container. The value of β for each chemical component can be estimated from the linear approximation $\rho_x = \rho_0(1 + \beta_x C_x)$, where ρ_0 is the density of water. The known values for the density ρ_x (g/cm^3) of chemicals at concentrations of C_x (M) in water were taken from the literature.[25−27] Then, the fitting parameter β_x (M^{-1}) is set to yield the value of ρ_x reported in the literature.

The simulation domain is a rectangular box $\Omega = \{(x,y,z){:}0 \leq x \leq L_x, 0 \leq y \leq H, 0 \leq z \leq L_z\}$ with horizontal dimensions L_x, L_z and height H. The fluid motion is described by the velocity $\mathbf{u} = (u_x, u_y, u_z)$ and pressure p; the concentration field of chemical j is given as C^j. The respective governing equations are the continuity, Navier−Stokes (in the Boussinesq approximation[24] and reagent diffusion equations)

$$\nabla\cdot\mathbf{u} = 0 \tag{2}$$

$$\frac{\partial\mathbf{u}}{\partial t} + (\mathbf{u}\cdot\nabla)\mathbf{u} = -\frac{1}{\rho_0}\nabla p + \nu\nabla^2\mathbf{u} - \mathbf{g}\frac{\Delta\rho}{\rho_0} \tag{3}$$

$$\frac{\partial C^j}{\partial t} + (\mathbf{u}\cdot\nabla)C^j = D^j\nabla^2 C^j + Q^j \tag{4}$$

where ∇ is the spatial gradient operator, ν is the kinematic viscosity, D^j is the diffusivity of respective reactants C^j, and Q^j is the corresponding source term describing the production or decomposition of chemicals during chemical reactions.

The no-slip boundary condition for the fluid velocity and zero chemical fluxes is imposed over all boundaries $\partial\Omega$ of the simulation domain

$$\mathbf{u}(\partial\Omega) = 0, \;\; \mathbf{n}\cdot\nabla C^j = 0, \;\; j = 1 \ldots N_C \tag{5}$$

Here, $\mathbf{n}$ is the unit normal vector at the boundary pointing into the fluid domain. To generate fluid motion, we use the following enzymatic reactions

$$\text{D-glucose} + O_2 \xrightarrow{\text{GOx}} \text{gluconic acid} + H_2O_2 \tag{R1a}$$

$$2H_2O_2 \xrightarrow{\text{CAT}} 2H_2O + O_2 \tag{R1b}$$

$$\text{PNPP} \xrightarrow{\text{AP}} \text{PNP} + NaH_2PO_4 \tag{R2}$$

Here, PNPP (see Figure 1 in the manuscript) stands for p-nitrophenylphosphate hexahydrate (disodium salt) $C_6H_4NO_6P{\cdot}2Na{\cdot}6H_2O$, and PNP denotes p-nitrophenol ($C_6H_5NO_3$). In modeling reaction R1a (where transformation of D-glucose into gluconic acid and hydrogen peroxide is catalyzed by glucose oxidase (GOx)) and reaction R1b (where decomposition of hydrogen peroxide is catalyzed by catalase (CAT)), we ignore the presence of oxygen because its expansion coefficient is much smaller than that of hydrogen peroxide.[19,20] Water is treated as a solvent with the density ρ_0. Setting $N_C = 6$, the concentrations of six chemicals participating in reactions R1a,R1b, and RRR2 are denoted $C^1 = [C_6H_{12}O_6]$, $C^2 = [C_6H_{12}O_7]$, $C^3 = [H_2O_2]$, $C^4 = [\text{PNPP}]$, $C^5 = [\text{PNP}]$, and $C^6 = [NaH_2PO_4]$. The respective values of each chemical required to determine the volumetric solutal expansion coefficient have been given in Table S1 (SI).[25−27]

Catalytic chemical reactions were modeled using the Michaelis−Menten reaction rates

$$r^j = \frac{r_{\max} C^j}{K_M + C^j} \tag{6}$$

controlled by the corresponding maximal reaction rate $r_{\max} = k_{\text{cat}}[\text{E}]$, which incorporates the reaction rate per molecule of enzyme k_{cat} and the enzyme concentration [E] (Table S2 in the Supporting Information), and the Michaelis constant K_M. The reactions involving $N_C = 6$ chemicals are catalyzed at the first pump, P_{GOx}, (see Figure 1), by glucose oxidase (GOx) with parameters $k_{\text{cat}}^{\text{R1a}} = k_{\text{cat}}^{\text{GOx}}$, $K_M^{\text{R1a}} = K_M^{\text{GOx}}$, $[\text{E}^{\text{R1a}}] = [\text{GOx}]$. Reactions at the second pump, P_{CAT}, are catalyzed by catalase (CAT) with parameters $k_{\text{cat}}^{\text{R1b}} = k_{\text{cat}}^{\text{CAT}}$, $K_M^{\text{R1b}} = K_M^{\text{CAT}}$, $[\text{E}^{\text{R1b}}] = [\text{CAT}]$. At the third pump, P_{AP}, the reactions are catalyzed by acid phosphatase (AP) with parameters $k_{\text{cat}}^{\text{R2}} = k_{\text{cat}}^{\text{AP}}$, $K_M^{\text{R2}} = K_M^{\text{AP}}$, $[\text{E}^{\text{R2}}] = [\text{AP}]$. The respective values for each of the enzymatic kinetic parameters are given in Table S2 in the Supporting Information.[10,28]

Assuming that the chemical reactions occur only at the surfaces of the three cylindrical gel pieces (pumps) P_{GOx}, P_{CAT}, and P_{AP}, soaked with the corresponding reactants and enzymes, we define source terms in eq 4 as

$$Q^j(\partial P_i) = r^j, \quad i = \text{GOx,CAT, AP} \tag{7}$$

where the boundaries of the pumps are defined as

$$\partial P_i(x_i, z_i) = \{(x, y, z)\colon (x - x_i)^2 + (z - z_i)^2 = R,\ 0 \le z \le H\},$$
$$i = \text{GOx, CAT, AP} \tag{8}$$

Here, R is the radius of the gel cylinder. At the gel boundaries, we require no-slip conditions for the fluid velocity: $\mathbf{u}(\partial_{Pi}) = \mathbf{0}$. The specific initial conditions are specified below for each set of simulations.

The physical mechanisms driving fluid motion can be elucidated if the Navier–Stokes eq 3 is recast in terms of the following nondimensional variables (denoted by primes)

$$\mathbf{r}' = \frac{\mathbf{r}}{L},\ t' = \frac{\nu t}{L^2},\ \mathbf{u}' = \frac{L\mathbf{u}}{\nu},\ p' = \frac{L^2}{\nu^2 \rho_0} p,\ C'^j = \frac{C^j}{C_0} \tag{9}$$

These variables are defined relative to the characteristic scales of the system: length L, time L^2/ν, and chemical concentration C_0. Omitting the primes, the equation becomes

$$\frac{\partial \mathbf{u}}{\partial t} + (\mathbf{u}\cdot\nabla)\mathbf{u} = -\nabla p + \nabla^2 \mathbf{u} - \mathbf{e}_y \sum_{j=1}^{N^C} \text{Gr}^j C^j \tag{10}$$

where $\mathbf{e}_y$ is a unit vector in the direction of gravity $\mathbf{g}$. The dimensionless solutal Grashof numbers are given by $\text{Gr}^j = \frac{g\beta_C^j L^4}{\nu^2}\frac{\text{d}C_0}{\text{d}x}$ and defined as ratios between the buoyancy and viscous forces. The Grashof number explicitly shows the scaling properties of the buoyancy forces due to the presence of the solutes characterized by the concentration C_0. The force is linearly proportional to the expansion coefficients β_C^j, the characteristic concentration gradient $\frac{\text{d}C_0}{\text{d}x}$, and to the fourth power of the characteristic length scale of the problem L (which could be a height of the chamber in our case). The force is also proportional to the dimensionless concentrations of the respective solutes C^j, which appear in (eq 10) as prefactors of the corresponding Grashof numbers Gr^j. These properties indicate that the buoyancy force depends not only on the presence of particular solutes (characterized by β_C^j) and their amounts (characterized by C_0) but also on the size of the of the chamber (characterized by L) and the chemical gradients developed within the system. These considerations can guide the design of the fluidic systems. For instance, the increase of the buoyancy forces, along with the resulting fluid velocities, can be achieved by increasing one of the characteristic parameters β_C^j, C_0, or L, while keeping the other two fixed.

The solutal buoyancy mechanism discussed in the manuscript can improve the efficiency of the transport properties of the fluidic systems. For example, based on the purely diffusive transport (characterized in one-dimensional by the relation $l^2 = 2Dt$), a chemical species with a diffusion coefficient $D \sim 10^{-9}$ m^2/s (relevant to the solutes considered in our study) traverses the distance $l = 1$ mm (relevant to the geometries of microfluidic devices) within the time $t \sim 10^3$ s. For micron-scale particles (biological cells with the diameter of tens of microns), the diffusion coefficients decrease to $D \sim 10^{-13}$ m^2/s (or 10^{-14} m^2/s), which increase the respective times required for the diffusive transport across the same distance up to 10^7 s (10^8 s). On the other hand, if convective transport advects immersed species (chemicals or particles) with a fluid velocity ∼10 μm/s, the cargo can be delivered across the distance within 10^2 s, which is an order of magnitude improvement over chemical diffusion and several orders of magnitude improvement over the diffusive transport of cargo (spores, particles, and biocells).

RESULTS AND DISCUSSION

Fabrication and Operation of the Enzymatic Pumps. The enzymatic pumps were fabricated by immobilizing the enzymes within cylindrical pieces of agarose gel (3%) with radius 2.5 mm and height 0.9 mm (see Experimental Section for details). Glucose oxidase is immobilized in the P_{GOx} gel, which also encapsulates *p*-nitrophenylphosphate (PNPP); catalase (CAT) is immobilized in the P_{CAT} gel, and acid phosphatase (AP) is fixed in the P_{AP} gel. The amounts of GOx, CAT, and AP loaded inside the gel were 2.8 (56), 0.5 (10), and 8 (160) μM (pmol), respectively. The pumps, in the triangular configuration (with distances P_{GOx}–P_{CAT} (P_{AP}) and P_{CAT}–P_{AP} being 6 and 7 mm, respectively), were placed into a cylindrical chamber with a radius of 1 cm and height of 0.9 mm (Figure 1a). After adding an aqueous solution of D-glucose into the chamber, the chemical reaction R1a, catalyzed by GOx, produces hydrogen peroxide and gluconic acid. Simultaneously, the PNPP encapsulated in the pump is released. Once, the chemically generated fluid flows reach pumps P_{CAT} and P_{AP}, reactions R1b and RRR2 (see schematic in Figure 1) are catalyzed, respectively. After PNPP is completely released from P_{GOx} and the catalytic reactions R1a, RRR1b, and RRR2 are complete, the system reaches an equilibrium where all chemical products are uniformly distributed throughout the domain and there is no fluid motion. Therefore, the time during which our system operates is set by the rate at which PNPP is released from the P_{GOx}-pump and the rates of catalytic reactions R1a, RRR1b, and RRR2, which fuel the fluid motion. The equilibrium is reached approximately after 4–5 h, but because the produced fluid flows maintain velocities on the order of few microns per second and the discussed flow bifurcation is clearly observed within first 2 h, we limit our experiments and simulations to the period of 120 min. To test the flow generated by each pump, polystyrene sulfate beads, 2 μm in diameter (Polysciences Inc.), were dispersed into the buffered or substrate containing solution inside the sealed chamber (these tracer particles simply follow the flow). The velocity of the generated flows was measured at 200 μm above the bottom surface at different distances away from the pumps and at different time intervals.

As detailed in the Experimental Section, the dynamics of the fluid and dissolved chemicals (of concentrations C_i) was modeled by solving the continuity, Navier–Stokes, and reaction-diffusion equations for the system.[23,24] Within the Navier–Stokes equation, we explicitly account for the solutal buoyancy force $\mathbf{f} = \mathbf{g}\rho_0 \sum \beta_i C_i$, which depends on gravity $\mathbf{g}$, solvent density ρ_0, and relevant expansion coefficients β_i.

We first investigated the individual behavior of each pump containing one of the enzymes (GOx, CAT, or AP) in the presence of the corresponding substrates (D-glucose, hydrogen

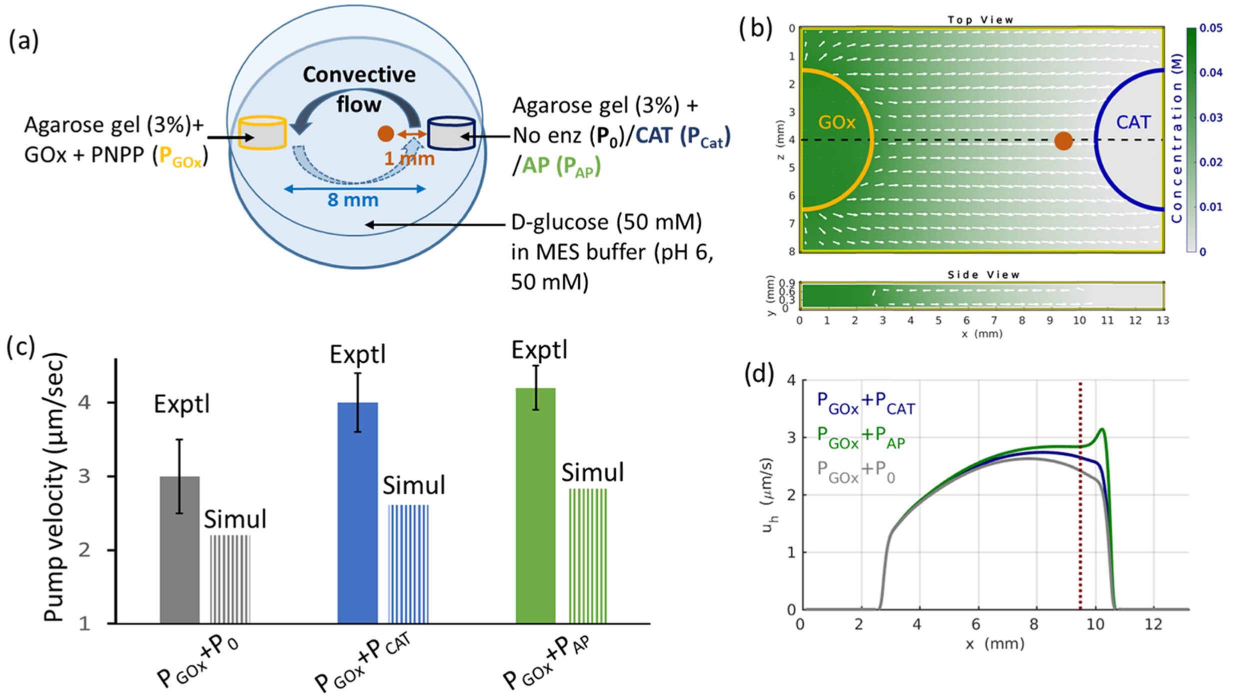

Figure 2. (a) Schematic of the experimental setup for the two-pump system including P_{GOx} and P_0/P_{CAT}/P_{AP} (orange and blue cylinders). (b) Top and side views of the simulation domain used to model the double-pump system (P_{GOx}−P_{CAT}). On the top view, white arrows show the directions of fluid velocity $u_h = (u_x^2 + u_z^2)^{1/2}$ in the plane $y = 0.2$ mm and on the side view, in the plane $z = 4$ mm. The green color shows the concentration of hydrogen peroxide at 120 min. Orange and blue semicircles indicate walls of P_{GOx} and P_{CAT} pumps (see also Supporting Information Video SV2). (c) Fluid velocities experimentally observed (also compared with their corresponding simulated value) at 120 min in front of the second pump (red dot in the schematic (a)); P_0, P_{CAT}, or P_{AP}, are shown with gray, blue, and green colors, respectively. Experimental condition: MES buffer (pH 6, 50 mM), agarose gel (3% with MES buffer), $[GOx]_{gel} = 2.8\ \mu M$, [D-glucose] = 50 mM, $[PNPP]_{gel} = 55.5$ mM, $[AP]_{gel} = 8\ \mu M$, $[CAT]_{gel} = 0.5\ \mu M$. The standard deviations shown are calculated for 10 tracer particles. (d) Simulated horizontal fluid velocities u_h in the central plane ($z = 4$ mm and $y = 0.2$ mm) are shown with gray, blue, and green lines for pumps P_{GOx}−P_0, P_{GOx}−P_{CAT}, and P_{GOx}−P_{AP}, respectively.

peroxide, or PNPP). For each enzymatic pump, an inward flow was observed, i.e., the solution flows toward the enzyme-containing gel along the bottom surface of the chamber and moves away from the gel along the top surface. The magnitude of the horizontal fluid velocity decreased with distance from the pump. After an initial transitional period, during which the flow spreads over the entire chamber, the pumps and generated flows were monitored for 1 h. Eventually, depletion of the fuel decreased the flow velocities (see Supporting Information Figures S2−S4 and Video SV1). In contrast, when 55 mM of PNPP was loaded into an enzyme-free gel submerged in a buffered-solution, an outward fluid flow (away from the pump) was generated due to the release of relatively dense PNPP out of the pump into the less dense solution.

When P_{GOx} was loaded with a mixture of GOx (2.8 μM) and PNPP (55 mM) and immersed into a D-glucose solution, the pump again generated an outward flow. Hence, the effects due to the leaching of PNPP out of P_{GOx} dominated over the inward flow produced due to the catalytic transformation of D-glucose. Thus, in the absence or presence of D-glucose, the PNPP-loaded P_{GOx} pump produced a net outward flow (see Supporting Information Figures S5 and S6). The velocities of the generated flows increase with the increasing concentrations of PNPP encapsulated in P_{GOx} (see Supporting Information Figure S5b−e) as a result of the increasing outflux of PNPP from P_{GOx} and because the buoyancy force, **f**, driving the flows, is proportional to the solute concentrations.[19]

We next used a double-pump system (see Figure 2, Supporting Information Figures S7, S8, and Video SV2) to investigate unidirectional flows produced by the exchange of chemicals between two pumps. Here, the first pump, P_{GOx}, always contained a mixture of GOx and PNPP. The second pump, placed 8 mm away from the P_{GOx}, contained either no enzyme (P_0), enzyme CAT (P_{CAT}), or AP (P_{AP}). A combination of P_{GOx} and P_0 pumps placed into D-glucose (or without it) produced an outward fluid flow (away from P_{GOx}) due to the leaching of PNPP out of P_{GOx} (the velocity profiles are shown in Supporting Information Figures S5 and S6). In contrast, the double pumps P_{GOx} + P_{CAT} and P_{GOx} + P_{AP} both provided a higher fluid velocity near the respective second pump (blue and green bars in Figure 2c). The elevated fluid velocities were produced by an additional inward flow (toward P_{CAT} or P_{AP}) generated by the decomposition of hydrogen peroxide catalyzed by CAT at P_{CAT} and by the transformation of PNPP catalyzed by AP in the case of P_{AP}. The increased velocities of flows directed from the P_{GOx} to the respective P_{CAT} and P_{AP} pumps (shown in Figure 2d) were observed after about 20 min, sufficient time for reactants generated at P_{GOx} to be transported (with an average speed ∼7 μm/s) to the respective P_{CAT} and P_{AP} pumps.

The combination of P_{GOx} and P_{CAT} pumps realizes a cascade of two sequential enzymatic reactions. First, GOx in P_{GOx} catalyzes the decomposition of D-glucose (that initially filled the chamber) into gluconic acid and hydrogen peroxide. Second, the H_2O_2 is transported by the generated flows to P_{CAT} and is decomposed into water and oxygen by the enclosed CAT (Figure 2b and Supporting Information Video SV2). In contrast, the combined action of P_{GOx} and P_{AP}

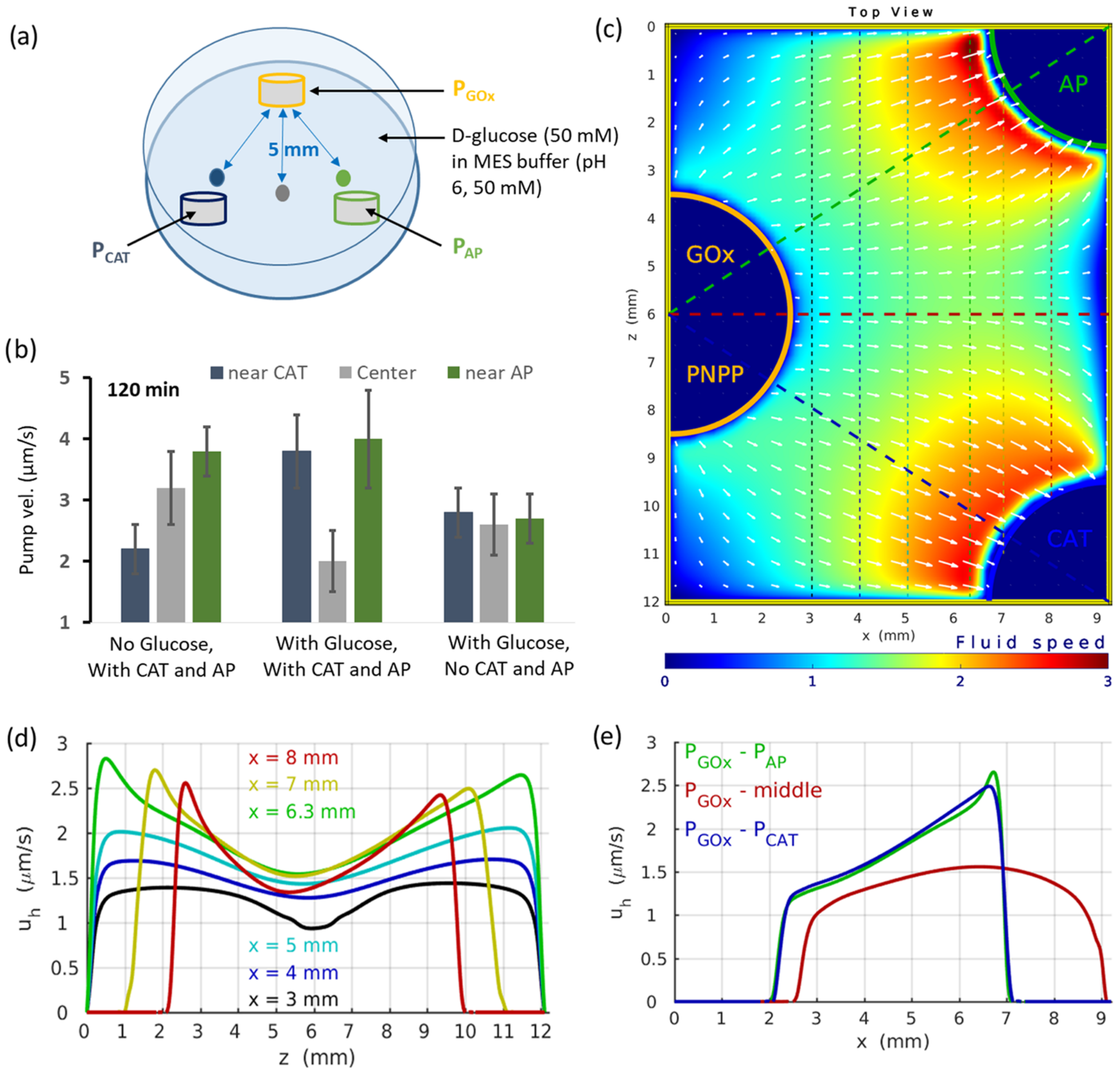

Figure 3. (a) Schematic of triple-pump experiments. (b) Pumping speed measured 5 mm away from the surface of P_{GOx} pump at positions marked by blue, gray, and green dots in the schematic (a). The flow speed was measured after 120 min in three different cases: (1) without glucose and with CAT and AP in P_{CAT} and P_{AP}, respectively; (2) with D-glucose and CAT and AP in P_{CAT} and P_{AP}, respectively; (3) with D-glucose but no CAT and AP in P_{CAT} and P_{AP}, respectively. The standard deviations shown are calculated for 10 tracer particles. (c) The color map of horizontal fluid velocities $u_h = (u_x^2 + u_z^2)^{1/2}$ (at $y = 0.2$ mm) illustrates bifurcating fluid flow directed from P_{GOx} to P_{CAT} and from P_{GOx} to P_{AP}, emphasized by yellow-to-red transitions. The magnitude of fluid velocities in μm/s is shown by the color-bar and directions by white arrows. (d, e) Velocity profiles $u_h(z)$and $u_h(x)$ illustrate the flow bifurcating along P_{GOx}−P_{CAT} and P_{GOx}−P_{AP} directions with velocities increasing toward P_{CAT} ($z = 12$ mm) and P_{AP} ($z = 0$ mm) pumps.

involves one noncatalytic reaction pathway, during which PNPP leaches out of P_{GOx}, generating fluid flow carrying PNPP to P_{AP}. At P_{AP}, the AP then catalyzes the decomposition of PNPP into PNP and NaH_2PO_4.

Three-Pump Network Generating the Bifurcating Flows. The double-pump systems suggest that chemicals can be transported from one pump to another by convective flows produced by either a cascade of enzymatic reactions or the leaching of a dense reactant (PNPP) in the solution. Importantly, the release of PNPP out of the gel P_{GOx} creates an outward flow (away from the pump), whereas uptake of the chemical into the second gel, P_{CAT} or P_{AP}, creates an inward flow. These observations informed our design of a three-pump network (shown in Figures 1 and 3) where the cascade reaction pathway, achieved through the chemical coupling between the P_{GOx} and P_{CAT} pumps, generates flow directed from P_{GOx} to P_{CAT}, and the noncascade pathway, realized between P_{GOx} and P_{AP} pumps, generates flow from P_{GOx} to P_{AP}. In Figure 1a, the distances from the P_{GOx} to P_{CAT} and P_{AP} pumps are 6 mm. The produced flows were observed after the addition of either buffer or glucose solution (see Figure 3a,b, Supporting Information Figures S9−S19 and Videos SV3−SV6).

To pinpoint factors regulating the three-pump network, we performed the following experiments with all three gels present but not necessarily activated. First, with only a buffer and no D-glucose in the ambient solution, the P_{GOx} is catalytically inactive. Nonetheless, the PNPP diffuses radially outward from this reservoir and produces an outward flow. With enzyme AP loaded in P_{AP}, PNPP was catalytically decomposed into less dense components, and P_{AP} acted as a pump with the fluid speed reaching the highest value near the P_{AP}. Notably, in the absence of D-glucose, H_2O_2 is not formed and, therefore, no

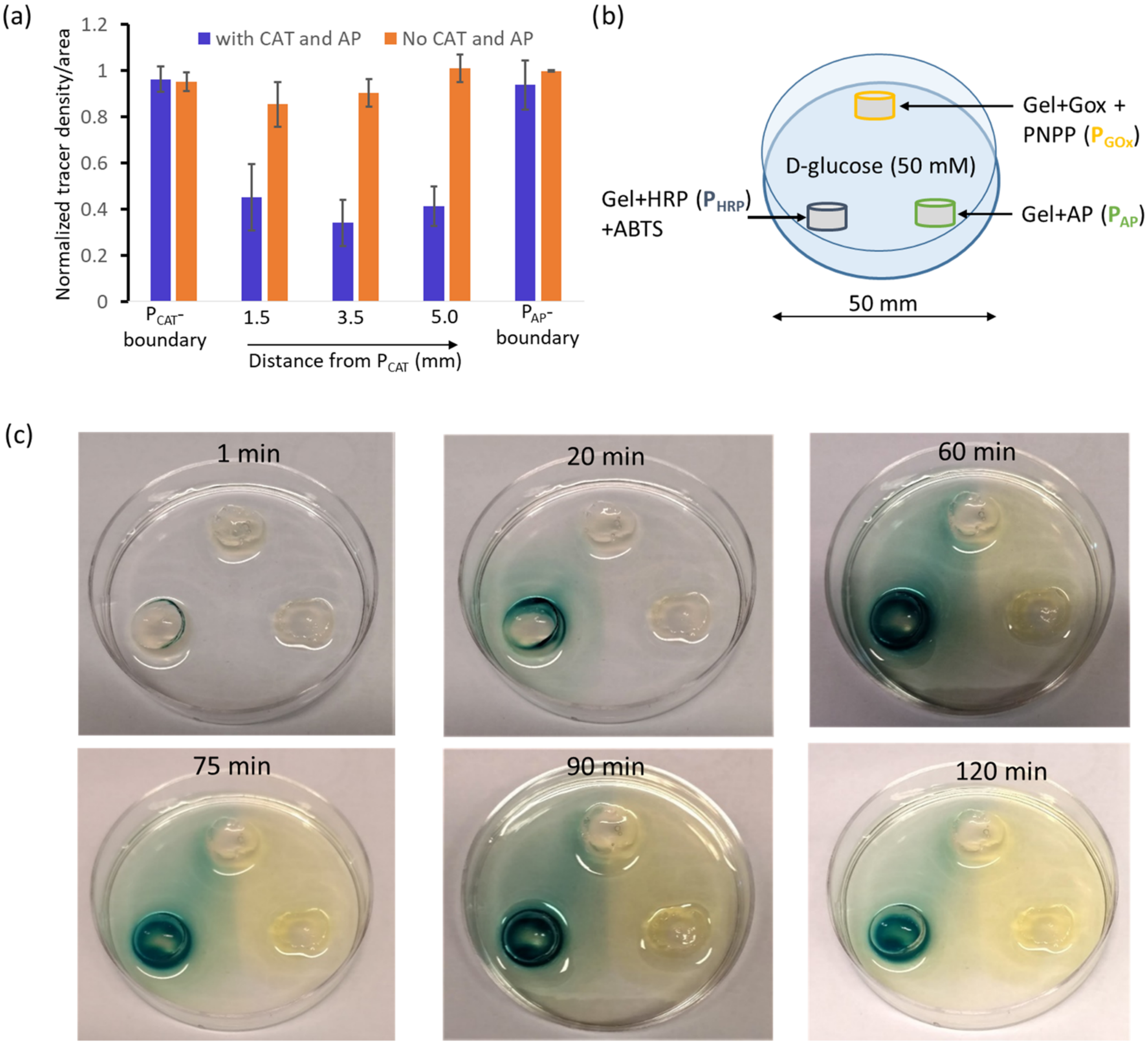

Figure 4. (a) Density distribution of 2 μm sPsL particles along P_{CAT} and P_{AP} axes in the absence and presence of CAT and AP in P_{CAT} and P_{AP} gel, respectively, in the presence of D-glucose. The number of particles settled on the surface was determined by the ImageJ software and then normalized. The standard deviations shown are calculated for three different experiments. (b, c) Visual detection of flow direction starting from GOx-containing gel to AP and HRP-containing gels at different time intervals. The blue color is due to the oxidation of ABTS by HRP and acts as an indicator for the flow direction between GOx and HRP-containing gel ($[GOx]_{gel}$ = 2.8 μM, $[PNPP]_{gel}$ = 55.5 mM, $[HRP]_{gel}$ = 5.5 μM, $[ABTS]_{gel}$ = 10 mM). The yellow color is due to the formation of PNP (hydrolyzed product of PNPP by AP), which also acts as the indicator for the flow direction between GOx and AP-containing gel.

enhanced pumping was detected near P_{CAT} (see Supporting Information Figures S18 and S19).

Second, in the presence of D-glucose in the ambient solution, the formation of H_2O_2 at P_{GOx}, with the subsequent catalytic decomposition of H_2O_2 by CAT at P_{CAT}, increased the fluid velocity near P_{CAT}. Enhanced pumping generating inward flow near P_{AP} was also observed due to the decomposition of PNPP. Notably, in the midpoint between the P_{CAT} and P_{AP} pumps, the flow velocity was much lower than near P_{CAT} or P_{AP} (see Figure 3b), again indicating that the fluid velocity is increased directly at the pump due to the inward flow (see Supporting Information Video SV6). With increasing concentration of PNPP (30, 55, and 100 mM PNPP) in the pump P_{GOx} the velocities generated near P_{CAT}, the center, and near P_{AP} also increase (see Supporting Information Figure S13). Faster fluid flows, generated from P_{GOx} with increasing PNPP, transport larger amounts of corresponding reactants (PNPP and H_2O_2), which then increases velocities generated by the secondary reactions catalyzed by the respective pumps P_{CAT} and P_{AP}. As previously reported, the pumping velocity of enzyme pumps increases with increasing substrate concentration.[19]

Third, as a control experiment, we monitored the flow behavior in a system containing D-glucose but lacking both CAT and AP. In this case, the fluid velocities along the different radial flow lines (marked in Figure 3a) are all comparable. Thus, the differential flow velocity along the P_{GOx}−P_{CAT} and P_{GOx}−P_{AP} lines in the presence of D-glucose is due to the flow bifurcation that originates from P_{GOx} (see Supporting Information Figure S14).

The simulations provide corroborating, quantitative data on the flow fields within the microchamber. The magnitude of the horizontal fluid velocity $u_h = (u_x^2 + u_z^2)^{1/2}$ is indicated by the color map in Figure 3c; the yellow-to-red transitions reveal the spatial development of two regions of high fluid velocities leading from P_{GOx} toward the P_{CAT} and P_{AP} pumps. The plots in Figure 3d,e further reveal that the fluid velocities are

DOI: 10.1021/acs.langmuir.8b03607
Langmuir 2019, 35, 3724−3732

significantly higher along lines connecting the P_{GOx}−P_{CAT} (dashed blue line in Figure 3c) and P_{GOx}−P_{AP} (dashed green line) pumps than between these two radial directions (dashed red line). In particular, the curves in Figure 3d show the fluid velocities for different values of the lateral distance, *x*, from P_{GOx} (dashed vertical lines in Figure 3c). Finally, the higher velocities along the P_{GOx}−P_{CAT} (blue) and P_{GOx}−P_{AP} (green) directions are compared to the velocity between the pumps (in the red direction) in Figure 3e.

The directed delivery of the sPsL tracer particles (whose specifications are given in the Experimental Section and SI) enabled by the generated flow illustrates a particularly useful attribute of the device. Initially, the tracers were uniformly dispersed throughout the chamber with most of the particles having settled at the bottom of the chamber within 2 h. In the presence of D-glucose in solution and CAT and AP in P_{CAT} and P_{AP}, respectively, the particles primarily concentrated near P_{CAT} and P_{AP}, with relatively low concentrations between the two pumps (Figure 4a). Importantly, when enzymes CAT and AP were not present in the respective gels, the distribution of tracers remained uniform (see Figure 4a and Supporting Information Figure S20).

The self-organized flow bifurcation is readily visualized in the 5 cm wide Petri dish in Figure 4c (see Experimental Section and SI for experimental details). To introduce color into the chemical solution, we designed the pump P_{HRP}, where along with horseradish peroxidase (HRP) (which is an oxidoreductase enzyme with H_2O_2 as a substrate), we added 2,2′-azino-bis(3-ethylbenzothiazoline-6-sulfonic acid) diammonium salt (ABTS), which converts to a blue product upon oxidation.[29] In contrast, in the vicinity of P_{AP}, PNPP will form the yellow-colored PNP by the catalytic action of AP. As shown in Figure 4c, distinct regions of blue and yellow are observed, reflecting the two flows P_{GOx}−P_{HRP} (blue) and P_{GOx}−P_{AP} (yellow). The sharp dividing line between the two regions further attests to the localized nature of the flow fields.

■ CONCLUSIONS

In summary, using theory and experiment, we demonstrate that the presence of multiple, immobilized enzymes in a fluid-filled chamber generates flows that spontaneously interact to form directed streams. In other words, the enzymatic pumps drive the organization of the self-generated flows into controllable fluidic circuits. Here, we used a triangular arrangement of three porous gels to generate two independent flow streams directed in distinct directions. The gels can, however, encapsulate different enzymes and be placed at different locations inside a chamber to create many other flow patterns, including feedback flow loops. Hence, this system can provide a new window into the dynamic interplay between chemistry and flow at the microscale. Notably, enzymatic reactions are ubiquitous in biological fluidic environments; in light of our findings, it can be important to consider if these catalytic reactions are producing local hydrodynamic behavior that, in turn, affects the local biological processes.[30,31]

These studies also facilitate technological applications of lab-scale fluidic devices. Namely, the controllable, directional flows permit the targeted delivery of chemicals and particles in the microchambers without the need for confining channels and thus can simplify device fabrication. Moreover, since the fluidic circuits are self-organized, the materials processing in the devices can be automated, requiring less intervention to regulate flow. The facile, active transport of reagents to different spatial locations has potential applications in the areas of programmable chemical synthesis,[32] spatial self-assembly of complex structures,[33−35] and microdevices for sensitive, point-of-care assays.[36]

■ ASSOCIATED CONTENT

Ⓢ Supporting Information

The Supporting Information is available free of charge on the ACS Publications website at DOI: 10.1021/acs.langmuir.8b03607.

Fabrication of the enzymatic pumps; experimental details of the flows generated by the single, double, and triple pumps; numerical modeling (PDF)

Depletion of the fuel (AVI)

Unidirectional flows produced by the exchange of chemicals between two pumps (AVI)

Produced flows observed on addition of either buffer or glucose solution (AVI) (AVI) (AVI) (AVI)

■ AUTHOR INFORMATION

Corresponding Authors

*E-mail: balazs@pitt.edu (A.C.B.).
*E-mail: asen@psu.edu (A.S.).

ORCID

Anna C. Balazs: 0000-0002-5555-2692
Ayusman Sen: 0000-0002-0556-9509

Author Contributions

§S.M. and O.E.S. contributed equally to this work.

Notes

The authors declare no competing financial interest.

■ ACKNOWLEDGMENTS

The work was supported by the Center for Chemical Innovation funded by the National Science Foundation (CHE-1740630).

■ REFERENCES

(1) Plutschack, M. B.; Pieber, B.; Gilmore, K.; Seeberger, P. H. The Hitchhiker's Guide to Flow Chemistry. *Chem. Rev.* **2017**, *117*, 11796−11893.

(2) Wegner, J.; Ceylan, S.; Kirschning, A. Ten Key Issues in Modern Flow Chemistry. *Chem. Commun.* **2011**, *47*, 4583−4592.

(3) Whitesides, G. M. The Origins and the Future of Microfluidics. *Nature* **2006**, *442*, 368−373.

(4) Guha, R.; Mohajerani, F.; Collins, M.; Ghosh, S.; Sen, A.; Velegol, D. Chemotaxis of Molecular Dyes in Polymer Gradients in Solution. *J. Am. Chem. Soc.* **2017**, *139*, 15588−15591.

(5) Kim, H.; Min, K. I.; Inoue, K.; Im, D. J.; Kim, D. P.; Yoshida, J. Submillisecond Organic Synthesis: Outpacing Fries Rearrangement Through Microfluidic Rapid Mixing. *Science* **2016**, *352*, 691−694.

(6) Wu, F.; Dekker, C. Nanofabricated Structures and Microfluidic Devices for Bacteria: From Techniques to Biology. *Chem. Soc. Rev.* **2016**, *45*, 268−280.

(7) Wang, H.; Wang, W.; Li, L.; Zhu, J.; Wang, W.; Zhang, D.; Xie, Z.; Fuchs, H.; Lei, Y.; Chi, L. Surface Microfluidic Patterning and Transporting Organic Small Molecules. *Small* **2014**, *10*, 2549−2552.

(8) Riahi, R.; Tamayol, A.; Shaegh, S. A. M.; Ghaemmaghami, A. M.; Dokmeci, M. R.; Khademhosseini, A. Microfluidics for Advanced Drug Delivery Systems. *Curr. Opin. Chem. Eng.* **2015**, *7*, 101−112.

(9) Mark, D.; Haeberle, S.; Roth, G.; Stetten, F. V.; Zengerle, R. Microfluidic Lab-on-a-Chip Platforms: Requirements, Characteristics and Applications. *Chem. Soc. Rev.* **2010**, *39*, 1153−1182.

(10) Sengupta, S.; Patra, D.; Ortiz-Rivera, I.; Agrawal, A.; Shklyaev, S.; Dey, K. K.; Cordova-Figueroa, U.; Mallouk, T. E.; Sen, A. Self-Powered Enzyme Micropumps. *Nat. Chem.* **2014**, *6*, 415−422.

(11) Ortiz-Rivera, I.; Shum, H.; Agrawal, A.; Sen, A.; Balazs, A. C. Convective Flow Reversal in Self-Powered Enzyme Micropumps. *Proc. Natl. Acad. Sci. U.S.A.* **2016**, *113*, 2585−2590.

(12) Kline, T. R.; Paxton, W. F.; Wang, Y.; Velegol, D.; Mallouk, T. E.; Sen, A. Catalytic Micropumps: Microscopic Convective Fluid Flow and Pattern Formation. *J. Am. Chem. Soc.* **2005**, *127*, 17150−17151.

(13) Valdez, L.; Shum, H.; Ortiz-Rivera, I.; Balazs, A. C.; Sen, A. Solutal and Thermal Buoyancy Effects in Self-Powered Phosphatase Micropumps. *Soft Matter* **2017**, *13*, 2800−2813.

(14) Sengupta, S.; Spiering, M. M.; Dey, K. K.; Duan, W.; Patra, D.; Butler, P. J.; Astumian, R. D.; Benkovic, S. J.; Sen, A. DNA Polymerase as a Molecular Motor and Pump. *ACS Nano* **2014**, *8*, 2410−2418.

(15) Zhang, H.; Duan, W.; Lu, M.; Zhao, X.; Shklyaev, S.; Liu, L.; Huang, T. J.; Sen, A. Self-Powered Glucose-Responsive Micropumps. *ACS Nano* **2014**, *8*, 8537−8542.

(16) Jun, I. K.; Hess, H. A biomimetic, Self-Pumping Membrane. *Adv. Mater.* **2010**, *22*, 4823−4825.

(17) Zhou, C.; Zhang, H.; Lia, Z.; Wang, W. Chemistry Pumps: a Review of Chemically Powered Micropumps. *Lab Chip* **2016**, *16*, 1797−1811.

(18) Guha, R.; Mohajerani, F.; Mukhopadhyay, A.; Collins, M. D.; Sen, A.; Velegol, D. Modulation of Spatiotemporal Particle Patterning in Evaporating Droplets: Applications to Diagnostics and Materials Science. *ACS Appl. Mater. Interfaces* **2017**, *9*, 43352−43362.

(19) Das, S.; Shklyaev, O. E.; Altemose, A.; Shum, H.; Ortiz-Rivera, I.; Valdez, L.; Mallouk, T. E.; Balazs, A. C.; Sen, A. Harnessing Catalytic Pumps for Directional Delivery of Microparticles in Microchambers. *Nat. Commun.* **2017**, *8*, No. 14384.

(20) Shklyaev, O. E.; Shum, H.; Sen, A.; Balazs, A. C. Harnessing Surface-Bound Enzymatic Reactions to Organize Microcapsules in Solution. *Sci. Adv.* **2016**, *2*, No. e1501835.

(21) Sitt, A.; Hess, H. Directed Transport by Surface Chemical Potential Gradients for Enhancing Analyte Collection in Nanoscale Sensors. *Nano Lett.* **2015**, *15*, 3341−3350.

(22) Li, M.; Su, Y.; Zhang, H.; Dong, B. Light-Powered Direction-Controlled Micropump. *Nano Res.* **2018**, *11*, 1810−1821.

(23) Pojman, J. A.; Epstein, I. R. Convective Effects on Chemical Waves. 1. Mechanisms and Stability Criteria. *J. Phys. Chem.* **1990**, *94*, 4966−4972.

(24) Chandrasekhar, S. *Hydrodynamic and Hydromagnetic Stability*; Dover: New York, 1981.

(25) Haynes, W. M.; Lide, D. R. *CRC Handbook of Chemistry and Physics: A Ready-Reference Book of Chemical and Physical Data*; CRC Press: Boca Raton, FL, 2015.

(26) Luong, T. K. N.; Shestakova, P.; Mihaylov, T. T.; Absillis, G.; Pierloot, K. P.; Vogt, T. N. Multinuclear Diffusion NMR Spectroscopy and DFT Modeling: A Powerful Combination for Unraveling the Mechanism of Phosphoester Bond Hydrolysis Catalyzed by Metal-Substituted Polyoxometalates. *Chem. - Eur. J.* **2015**, *21*, 4428−4439.

(27) Larhed, A. W.; Artursson, P.; Grasjo, J.; Bjork, E. Diffusion of drugs in native and purified gastrointestinal mucus. *J. Pharm. Sci.* **1997**, *86*, 660−665.

(28) Kruzel, M.; Morawiecka, B. Acid phosphatase of potato tubers (*Solanum tuberosum* L.). Purification, properties, sugar, and amino acid composition. *Acta Biochim. Pol.* **1982**, *29*, 321−330.

(29) Ponhong, K.; Supharoek, S.; Siriangkhawut, W.; Grudpan, K. A Rapid and Sensitive Spectrophotometric Method for the Determination of Benzoyl Peroxide in Wheat Flour Samples. *J. Food Drug Anal.* **2015**, *23*, 652−659.

(30) Goldbeter, A. Dissipative Structures in Biological Systems: Bistability, Oscillations, Spatial Patterns and Waves. *Philos. Trans. R. Soc., A* **2018**, *376*, No. 20170376.

(31) Zhao, X.; Gentile, K.; Mohajerani, F.; Sen, A. Powering Motion with Enzymes. *Acc. Chem. Res.* **2018**, *51*, 2373−2381.

(32) Günther, A.; Jensen, K. F. Multiphase Microfluidics: From Flow Characteristics to Chemical and Materials Synthesis. *Lab Chip* **2006**, *6*, 1487−1503.

(33) Dobnikar, J.; Snezhko, A.; Yethiraj, A. Emergent Colloidal Dynamics in Electromagnetic Fields. *Soft Matter* **2013**, *9*, 3693−3704.

(34) Lee, H.; Kim, J.; Kim, H.; Kim, J.; Kwon, S. Colour-Barcoded Magnetic Microparticles for Multiplexed Bioassays. *Nat. Mater.* **2010**, *9*, 745−749.

(35) Katsikis, G.; Cybulski, J. S.; Prakash, M. Synchronous Universal Droplet Logic and Control. *Nat. Phys.* **2015**, *11*, 588−597.

(36) Zhang, Q.; Zhang, M.; Djeghlaf, L.; Bataille, J.; Gamby, J.; Haghiri-Gosnet, A. M.; Pallandre, A. Logic Digital Fluidic in Miniaturized Functional Devices: Perspective to the Next Generation of Microfluidic Lab-on-Chips. *Electrophoresis* **2017**, *38*, 953−976.

DOI: 10.1021/acs.langmuir.8b03607
Langmuir 2019, 35, 3724−3732